Steel and Composite Structures, *Vol. 36, No. 5 (2020) 507-519*
DOI: https://doi.org/10.12989/scs.2020.36.5.507

Effect of height-to-width ratio on composite wall under compression

Ying Qin*[1], Xin Yan[1], Guan-Gen Zhou[2] and Gan-Ping Shu[1]

[1]Key Laboratory of Concrete and Prestressed Concrete Structures of Ministry of Education, School of Civil Engineering, Southeast University, Nanjing, China
[2]Zhejiang Southeast Space Frame Group Company Limited, Hangzhou, China

(*Received March 16, 2019, Revised August 5, 2020, Accepted August 13, 2020*)

Abstract. Double skin composite walls are increasingly popular and have been applied to many safety-related facilities. They come from the concept of composite slabs. Conventional connectors such as shear studs and binding bars were used in previous studies to act as the internal mechanical connectors to lock the external steel faceplates to the concrete core. However, the restraint effects of these connectors were sometimes not strong enough. In this research, a recently proposed unique type of steel truss was employed along the wall height to enhance the composite action between the two materials. Concrete-filled tube columns were used as the boundary elements. Due to the existence of boundary columns, the restraints of steel faceplates to the concrete differ significantly for the walls with different widths. Therefore, there is a need to explore the effect of height-to-width ratio on the structural behavior of the wall. In the test program, three specimens were designed with the height of 3000 mm, the thickness of 150 mm, and different widths, to simulate the real walls in practice. Axial compression was applied by two actuators on the tested walls. The axial behavior of the walls was evaluated based on the analysis of test results. The influences of height-to-width ratio on structural performance were evaluated. Finally, discussion was made on code-based design.

Keywords: height-to-width ratio; composite wall; compressive loading; structural behavior; double skin

1. Introduction

Double skin steel-concrete-steel composite walls, which consist of two external steel faceplates and infilled concrete core, have been applied to many facilities such as safety-related nuclear containment, gravity seawalls, military shelters, offshore deck structures, and building core. Recently, this type of wall is also considered for possible applications in the future modular reactor plants (Seo *et al.* 2016). The noticeable inherent merit of this wall is that the external steel faceplates serve as both permanent formwork for casting concrete and primary reinforcement during the service stage. The load-carrying capacity significantly increases compared with pure steel frames (Hariri-Ardebili *et al.* 2014a, Mirtaheri and Zoghi 2016) and steel plate shear walls (Hajimirsadeghi *et al.* 2019). Furthermore, double skin composite walls are suitable and efficient for assembly construction techniques, which requires faster fabrication, construction and erection comparing to conventional reinforced concrete construction (Hariri-Ardebili *et al.* 2014b). The external steel faceplates are pre-fabricated in factories in the form of modules before delivering to the site for rapid installation, after that, the concrete is filled inside to form the composite walls. The feature of efficiency in construction and saving in time and cost makes the wall increasingly popular.

The composite action (i.e., the cooperative work) between concrete core and steel faceplates is achieved by using internal mechanical connectors to effectively lock the steel plates and concrete core together (Lee *et al.* 2019a, 2019b, Curkovic *et al.* 2019). Similar to the buckling-restrained braces (Mirtaheri *et al.* 2011, 2018, Gheidi *et al.* 2011), the early local buckling of steel plates can also be prevented if strong support from connectors has been provided (Qin *et al.* 2018, 2020a). Various types of connectors have been proposed by former researchers, such as binding bars (Prabha *et al.* 2013), headed studs (Yan *et al.* 2018), J-hook (Huang and Liew 2016), embedded cold-formed steel tubes (Hilo *et al.* 2016), ring stiffened tubes (Liao and Ma 2018), C-chanels (Yan *et al.* 2019), and combined transverse stiffeners and vertical diaphragm (Huang *et al.* 2018). These connectors offer mechanical advantages in terms of convenience for fabrication and ability to maintain structural integrity under compression.

An effective mechanical connector should prevent the possible separation between the steel faceplates and the concrete core under compressive loading. In addition, good performance is required under high level of compression. Ease of installation is another important issue that should be considered. After taking into account all these factors, a double skin composite wall system with steel truss connector was recently proposed (Qin *et al.* 2019a, b, c), as shown in Fig. 1. The steel truss is composed of two angles as the chord members and rebar as the web member. It is fillet welded to the steel faceplates along the wall height. Cold-formed tube columns are used as the boundary elements to enhance the structural response. The concrete is then filled both between the two steel faceplates and into the tube columns to construct the composite wall. Compared with conventional composite wall which

*Corresponding author, Associate Professor
E-mail: qinying@seu.edu.cn

http://www.techno-press.org/?journal=scs&subpage=8
ISSN: 1229-9367 (Print), 1598-6233 (Online)

provides point constraints (Guo and Zhao 2019), the truss connectors offer stronger line constraints to the steel faceplates along the wall height.

Eom *et al.* (2009) performed cyclic testing on three isolated and two coupled composite walls, and plastic stress distribution in concrete and steel cross-sectional area was used to calculate the load-bearing capacity. Luo *et al.* (2015) studied the influences of the concrete strength, the plate thickness, the height-to-width ratio, and the axial compression ratio on the ultimate load-carrying capacity and seismic behavior of composite walls. Zhao *et al.* (2016) employed a quadri-linear model to represent the hysteretic behavior of composite walls under cyclic in-plane loading. Nguyen and Whittaker (2017) used finite element models to study the key variables such as faceplate slenderness ratio, connector type, and reinforcement ratio in composite walls. Huang *et al.* (2018) experimentally investigated the seismic performance of an innovative composite walls with vertical diaphragms, transverse stiffeners, and distributed batten plates welded on steel faceplates.

Some work has been done on the compressive behavior of double skin composite walls. Choi *et al.* (2014) tested six wall specimens with the considered parameter of concrete type and width-to-thickness ratio of steel faceplates. Huang and Liew (2016) conducted compressive tests on composite walls with J-hook connectors. The method to predict the compressive resistance was proposed, which considered the influence of J-hook connectors on the lateral supports to steel faceplates. Qin *et al.* (2019d, e) investigated the influences of type of fastener and profiled steel sheet, arrangement of fastener, and boundary confinement on the compressive performance of profiled composite walls. However, most of the tested walls are short walls whose height-thickness ratio less than four. These walls are classified into short walls and the failure mode is governed by the cross-sectional capacity. In practical design, the height-to-thickness ratio for many walls are greater than eight and shall be considered as long walls. This means the walls are mostly possible to experience global instability. Recently, Qin *et al.* (2017) proposed equations to calculation the load-carrying capacity with the consideration of plate yielding. Meanwhile, the effects of height-to-thickness ratio, the truss spacing, and the faceplate thickness were studied by experimental investigations on both high walls (Qin *et al.* 2019a, b, f, b) and short walls (Qin *et al.* 2020c, d, e, f) with truss connectors.

Due to the existence of boundary columns, for the composite walls with the same height and thickness but different widths, the restraints to steel faceplates change significantly, which finally leads to the change in the composite action between the two materials. Therefore, this paper investigated the effect of height-to-width ratio on the structural performance of the double skin composite walls under compressive loading. Full-scale tests were conducted on three specimens with different height-to-width ratios. The test results were discussed in terms of failure modes, load-displacement response and strain distribution. The effect of height-width ratio was comprehensively discussed.

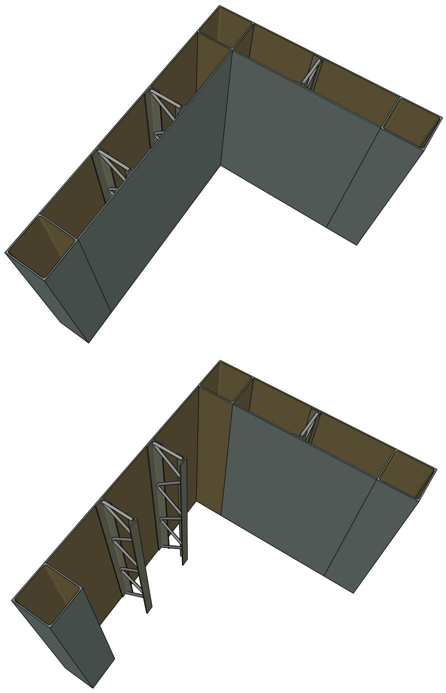

Fig. 1 Details of double skin composite wall

2. Experimental program

2.1 Test specimens

Three innovative specimens with different height-to-width ratios, labelled as SCW-2.0, SCW-2.5, SCW-3.2, were tested under axial compression. The numbers (2.0, 2.5, and 3.3) denote the corresponding height-to-width ratio of each specimen. The specimens were designed and manufactured at the full scale to represent the one-story height walls. Fig. 2 shows the detailed dimensions and configurations of the three test specimens. The height and thickness for all specimens were 3000 mm and 150 mm, respectively, while the width varied from 1500 mm to 900 mm, including two concrete-filled square tube columns with the cross-sectional area of 150×150 mm served as the boundary elements at the sides of the wall. The corresponding height-to-width ratio is 2.0, 2.5, and 3.3, respectively. The thickness of the steel tube and the steel faceplate was 4 mm. The steel truss, which was used to connect the two external steel faceplates at the inner space of each steel compartment, was composed of two angles with the cross-sectional dimension of 40×40×4 mm and kinked rebar with the diameter of 8 mm. The spacing of the steel truss was 200 mm, which met the requirement of limitation value of spacing-to-thickness ratio ($40\sqrt{235/f_y}$) based on the JGJ/T 380-2015 (2015) Chinese code for design of steel plate shear walls. The specimen was covered by a base plate and a top plate with the thickness of 30 mm for the convenience of installation.

2.2 Material properties

The strength grade of C25, whose characteristic cubic compressive strength is 25 MPa based on Chinese code for design of concrete structures (GB 50010-2010 2010), was selected for the infilled concrete core for all specimens Six cubes with the dimension of 150×150×150 mm were prepared to determine the actual cubic compressive strength. The average cubic compressive strength obtained from concrete test was 23.5 MPa.

The strength grade of Q235, whose nominal yield strength is 235 MPa according to Chinese code for design of steel structures (GB 50017-2017 2017), was chosen for all steel components for specimens. Four tensile coupons were fabricated for steel faceplates and tube columns from the same batch of the test specimens. According to the coupon tests, the actual average yield strength (f_y), ultimate strength (f_u), modulus of elasticity (E_s), and elongation (Elo) were 346.0 MPa, 364.8 MPa, 1.99×10^5 MPa, and 34%, respectively, for steel faceplates, and 261.6 MPa, 362.8 MPa, 2.05×10^5 MPa, and 31%, respectively, for tube columns.

2.3 Test setup and loading procedure

The axial compressive tests were conducted in the 20,000 multi-functional loading frame, as illustrated in Fig. 3. The base plate and top plate of the wall were connected to the foundation beam of loading frame and spreader beam by high-strength bolts, respectively. Four lateral supports were designed at the sides of spreader beam to prevent possible lateral movement during the test. The axial compressive loading was applied by a couple of 1,000 kN capacity hydraulic actuators. The compressive load was applied by using force control approach. A load interval of 363.64 kN was used during the test. The test was stopped when the axial compressive capacity of wall dropped below 85% of the peak load.

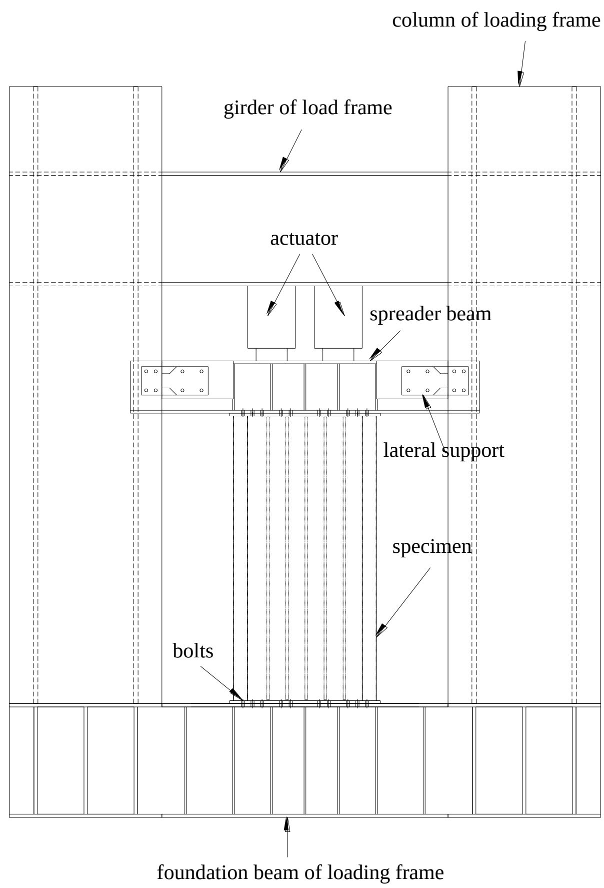

Fig. 3 Test setup

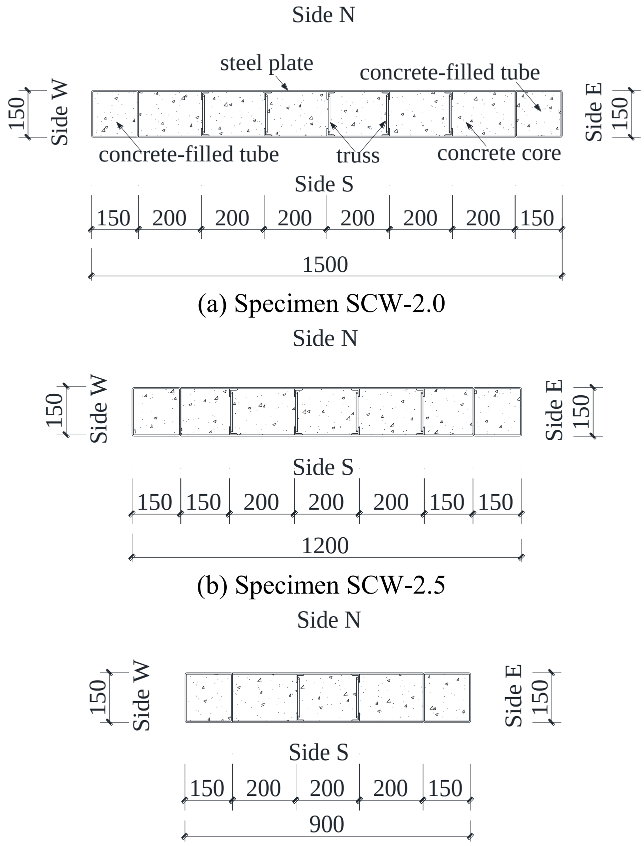

Fig. 2 Specimen details (dimension in mm)

2.4 Instrumentations

Linear variable differential transducers (LVDTs) were installed to measure the specimen deformation during the test, as shown in Fig. 4. The transducers W1-W2, W12-W13 were arranged at the top of wall along the vertical direction to monitor the axial displacement of the specimen under compression. Fourteen horizontal transducers (W3-W11, and W14-W18) were placed perpendicular to the wall face at the distance of 500 mm, 1000 mm, 1500 mm, 2000 mm from the wall base to measure the out-of-plane lateral deformation at different wall heights. In addition, one horizontal transducer was installed along the wall width at the middle height of the wall to monitor the possible in-plane lateral deformation. Strain gauges were placed on the steel faceplates and tube columns along the wall height to obtain the strain distribution, as shown in Fig. 5.

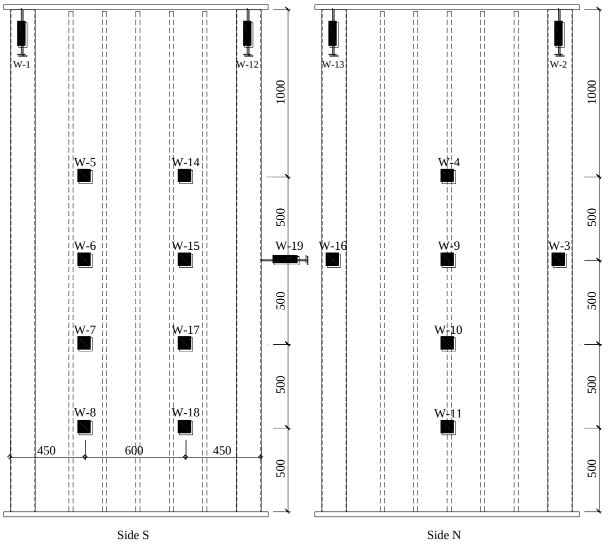

(a) Specimen SCW-2.0

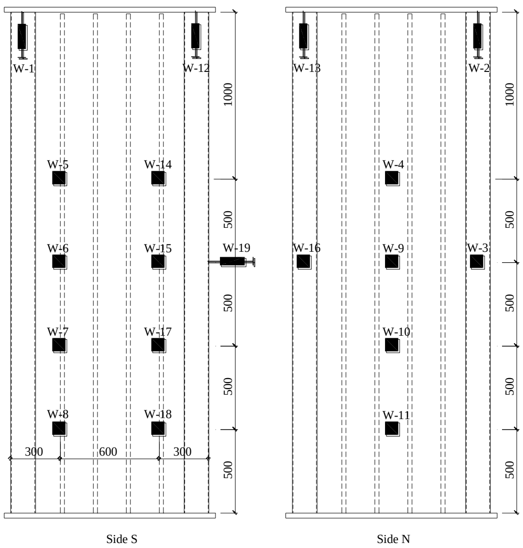

(b) Specimen SCW-2.5

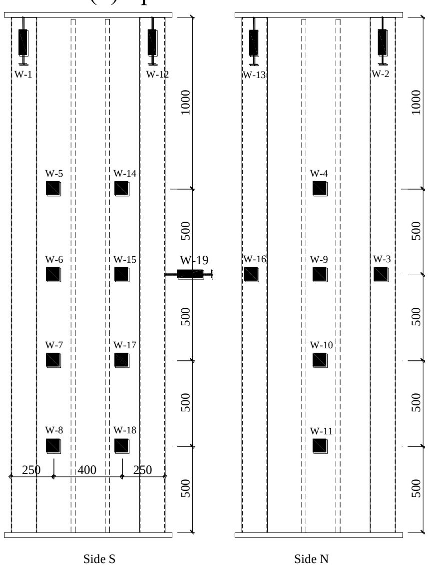

(c) Specimen SCW-3.3

Fig. 4 Arrangement of transducers

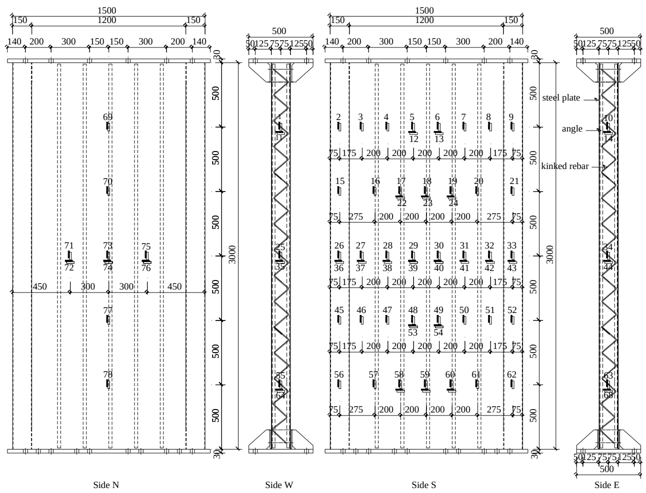

(a) Specimen SCW-2.0

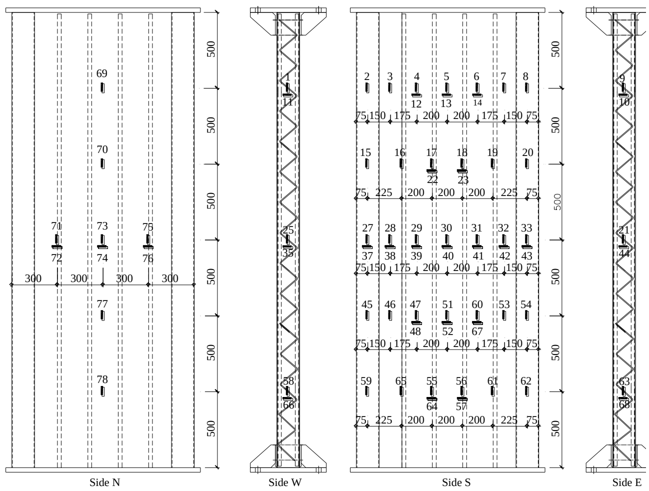

(b) Specimen SCW-2.5

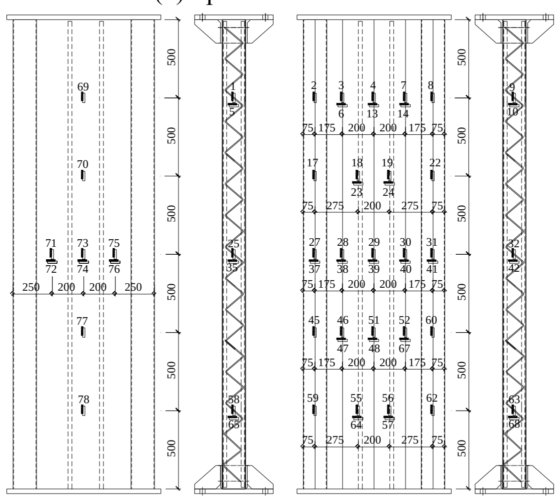

(c) Specimen SCW-3.3

Fig. 5 Arrangement of strain gauges

3. Experimental observation

As will be seen from the test observation described below, all specimens exhibited similar failure mode including the local buckling of steel faceplates before approaching the peak load, followed by the global instability of specimens, and the subsequent buckling of the boundary concrete-filled tube columns during the post-peak period.

Specimen SCW-2.0 behaved in a smooth manner during the beginning of axial loading. No obvious deformation or damage was observed until the axial load reached 4000 kN. When the load arrived at 4000 kN, slight local buckling was found in the region at a distance of 150 mm to 1000 mm from the wall base on side N, as shown in Fig. 6(a). As the load progressed to 5091 kN, similar buckling was observed in the region at a distance of 500 mm to 1000 mm from the wall base on side S. The buckling of steel plate on side N extended to the middle height of the wall at the loading level of 6545 kN. The buckled shape became more serious as the load continued to increase. The specimen suffered from global buckling when it reached its peak load of 8000 kN, as shown in Fig. 6(b). Simultaneously, the steel faceplate severely buckled at the distance of 150 mm to 600 mm from the top of wall, as shown in Fig. 6(c). Similar buckling was also found on the boundary elements. The failure of the specimen on side N was illustrated in Fig. 6(d).

Specimen SCW-2.5 behaved in a similar manner as Specimen SCW-2.0 did. There was no physical observation at the very beginning. At the loading level of 3636 kN, steel faceplate slightly buckled at a distance of 300 mm to 600 mm from the wall base on side N. The buckling was observed at the middle height of the wall on side N when the load arrived at 4727 kN. Meanwhile, slight buckling could be seen near the wall base on side S. As the load reached 5455 kN, the buckled shape on side N could be found in the lower half region of wall height. The buckling gradually extended to the upper half region of wall height as the load progressed to 6545 kN, as shown in Fig. 7(a). Continuous sound was emitted from the specimen at this loading level. The specimen experienced global buckling when the peak load of 7273 kN was achieved, as shown in Fig. 7(b). The failure of specimen on sides N and S were illustrated in Figs. 7(c) and 7(d), respectively.

(a) Slight buckling on side N

Continued-

(b) Severe buckling on side S

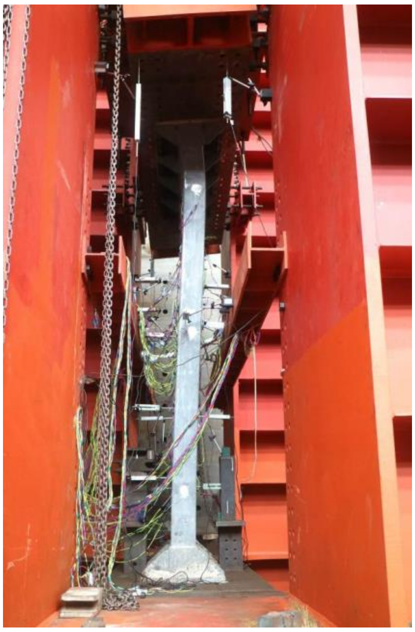

(c) Global buckling

(d) failure of specimen on side N

Fig. 6 Failure of Specimen SCW-2.0


(a) Buckling of upper half of wall height


(b) Failure on side E


(c) Failure on side N

Continued-


(d) Failure on side S

Fig. 7 Failure of Specimen SCW-2.5


(a) Failure on side S


(b) Failure on side N

Continued-

(c) Global buckling

Fig. 8 Failure of Specimen SCW-3.3

As for Specimen SCW-3.3, slight buckling was found at the distance of 1700 mm from the wall base on side S at the loading level of 4000 kN. As the load increased to 5091 kN, buckling was observed on both sides N and S at the middle height of the specimen. The buckling extended to the lower half height of wall when the axial load arrived at 5455 kN. The specimen reached its peak load when the load increased to 5818 kN. Global buckling was noticeable as shown in Fig. 8(c). Severe buckling could be seen at the distance of 150 mm to 700 mm from the top of wall on side N, as shown in Fig. 8(a). Serious buckling was also found at the distance of 150 mm to 500 mm from the top of wall on side S, as shown in Fig. 8(b). Meanwhile, both boundary tube columns bulged outwards near the wall top.

4. Test results

4.1 Load versus axial displacement response

4.1.1 Load-axial displacement curve

The load-axial displacement behavior of specimens with different height-to-width ratios is shown in Fig. 9. For Specimens SCW-2.0, SCW-2.5, and SCW-3.3, the peak loads are 8000 kN, 7273 kN, and 5818 kN, respectively. The axial displacements corresponding to the peak loads are 9.57 mm, 14.43 mm, and 14.25 mm. The capacity of walls with the width of 1500 mm and 1200 mm are increased by 37.5% and 25.0% over that of the specimen with the width of 900 mm. Considering the fact that the cross-sectional areas of Specimens SCW-2.0 and SCW-2.5 are 66.7% and 33.3% larger than that of Specimen SCW-3.3, the increase rate of capacity is slower than that of cross section. This is because the boundary concrete-filled tube columns provide better confinement to walls with narrower width, which increases the wall capacity. Furthermore, it could be seen that the wider wall shows smaller axial displacement under the same loading level, which indicates higher axial stiffness.

4.1.2 Buckling load

For double skin composite walls with thin steel faceplates, the steel faceplates tend to buckle outwards between the two adjacent steel trusses under axial compression. The strain will change suddenly at the buckling location. Therefore, the buckling strain can be determined by the inflection point on the load-strain curves.

Fig. 10 shows the partial enlarged drawings of load-strain curves for several strain gauges for the three specimens. The inflection points of the curves are labelled by red squares at the upper portion of the drawings. The curves in Fig. 10(a) shows that Specimen SCW-2.0 has a buckling strain of $-951\times10^{-6}\mu\varepsilon$, and the corresponding buckling stress and buckling load are 189.2 MPa and 2909 kN, respectively. For Specimen SCW-2.5, the buckling strain is $-569\times10^{-6}\mu\varepsilon$ as shown in Fig. 10(b), and the corresponding buckling stress and buckling load are 113.2 MPa and 2545 kN, respectively. As is evident from Fig. 10(c), Specimen SCW-3.3 has a buckling strain of $-469\times10^{-6}\mu\varepsilon$, and the corresponding buckling stress and buckling load are 93.3 MPa and 1818 kN, respectively.

It can be observe from Table 2 that, the ratios of buckling load N_b to peak load N_u of three specimens (N_b/N_u) range from 0.31 to 0.36. No obvious differences can be found among specimens. The steel faceplates can be considered as several rectangular plates in rigid contact with concrete while restrained by adjacent steel trusses. Since the ratio of truss spacing to plate thickness for three specimens is the same, it is expected that no obvious differences in N_b/N_u can be found. Therefore, it indicates that the height-to-width ratio does not affect the local buckling of steel faceplates.

Euler theory provides predictions for the elastic buckling stress $\sigma_{cr,Euler}$ in the buckled steel plate segments between adjacent trusses of double skin composite walls, as given by Eq. (1) (Choi *et al.* 2014).

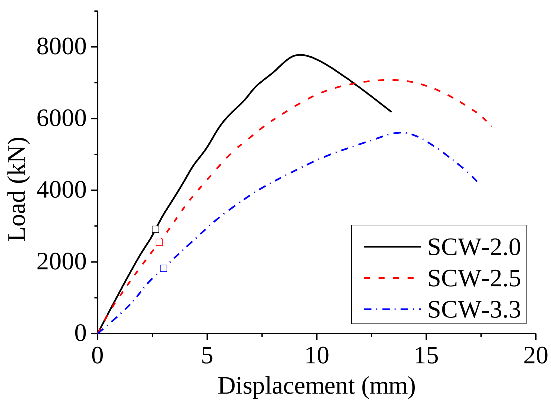

Fig. 9 Load versus axial displacement curves

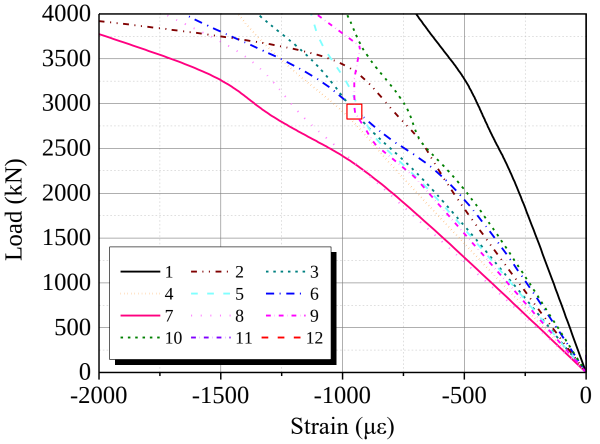

(a) Specimen SCW-2.0

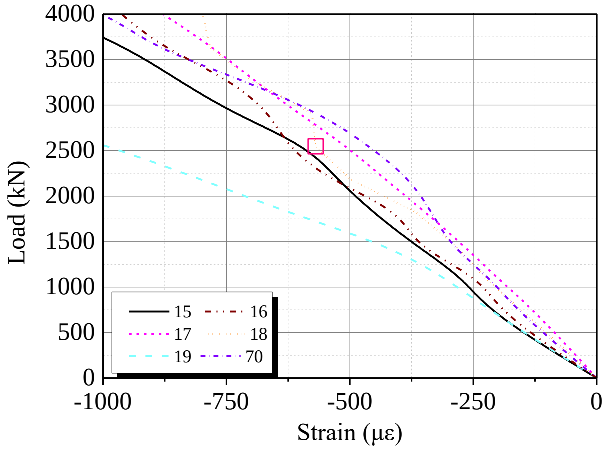

(b) Specimen SCW-2.5

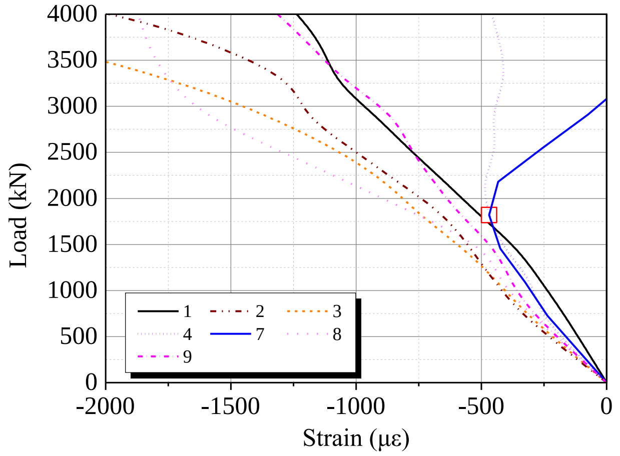

(c) Specimen SCW-3.3

Fig. 10 Buckling stress of specimens

$$\sigma_{cr,Euler} = \frac{\pi^2 E_s}{12k^2(\overline{B}/t)^2} \quad (1)$$

where k is the effective length factor, whose value can be taken as 1.0 for simply-supported case and 0.7 for clamped case; $\overline{B}$ is the spacing of steel trusses; and t is the thickness of steel faceplate.

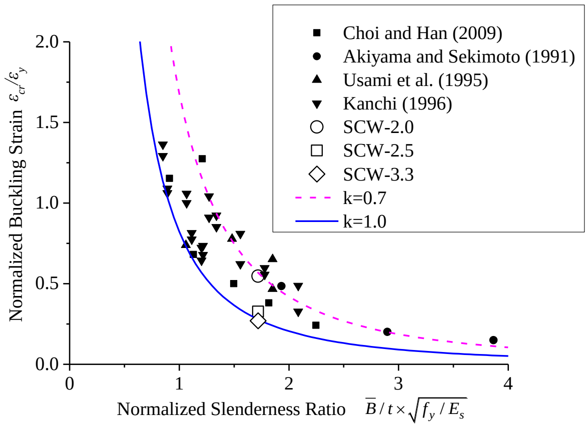

Fig. 11 Comparison with Euler curves

Axial compression tests have been performed by several researchers on double skin composite walls with different ratios of stud spacing to steel faceplate thickness (Akiyama and Sekimoto 1991, Usami *et al.* 1995, Kanchi 1996, Choi and Han 2009). Fig. 11 plots test results of the relationship between the normalized buckling strain $\varepsilon_{cr}/\varepsilon_y$ and normalized slenderness ratio $\overline{B}/t\times\sqrt{f_y/E_s}$ in these research. Meanwhile, the data for Specimens SCW-2.0, SCW-2.5, and SCW-3.3 are also plotted. It can be observed that the data of all three specimens are lying between the Euler curves with k=0.7 and k=1.0. It can also be found that the plots of specimen with greater height-to-width ratio is closer to the Euler curve with k=1.0. This is opposite to the observations for short walls (Qin *et al.* 2020c). This may be caused by the fact that the overall buckling of the high wall has certain effect on the boundary condition of steel faceplate.

4.1.3 Axial stiffness

Table 2 lists the buckling load N_b, buckling displacement δ_b, ultimate load N_u, ultimate displacement δ_u, $0.3N_u$ and the corresponding displacement $\delta_{0.3u}$, $0.6N_u$ and the corresponding displacement $\delta_{0.6u}$. The buckling load is also labelled by squares in the lower portions of the load-axial displacement curves in Fig. 9. It can be observed that the slope of curves does not change obviously after the specimens have reached the buckling load. This infers that the influence of plate buckling on stiffness of specimens is not significant.

In order to quantify the effect of local buckling on stiffness, two types of secant stiffness are employed. The first (K_b) uses the buckling load point as the starting point and the $0.6N_u$ point as the terminal point, while the second ($K_{0.3u}$) uses the $0.3N_u$ point as the starting point and the $0.6N_u$ point as the terminal point. As can be seen from Table 2, the values of $K_{0.3u}$ and K_b are closely corresponded. This further indicates that the axial stiffness does not obviously affected by the local buckling of faceplates. In addition, as is expected, the secant axial

Table 1 Stiffness calculation

Specimen No.	N_b	δ_b	N_u	δ_u	$\frac{N_b}{N_u}$	$0.3N_u$	$\delta_{0.3u}$	$0.6N_u$	$\delta_{0.6u}$	K_b	$K_{0.3u}$	$\frac{K_{0.3u}}{K_b}$
	kN	mm	kN	mm		kN	mm	kN	mm	kN/mm	kN/mm	
SCW-2.0	2909	2.65	8000	9.57	0.36	2400	2.15	4800	4.49	1028	1026	1.00
SCW-2.5	2545	2.82	7273	14.43	0.35	2182	2.35	4364	5.09	801	796	0.99
SCW-3.3	1818	3.02	5818	14.25	0.31	1745	2.88	3491	6.10	543	542	1.00

stiffness decreases with the increase in height-to-width ratio.

4.1.4 Ductility

Ductility (μ) is defined as the ability of specimens to undergo large plastic deformation without significant loss of capacity. It can be calculated by the ratio of the axial displacement corresponding to $0.85N_u$ (δ_m) to that corresponding to the yield strength N_y (δ_y). The method to determine the yield strength and the corresponding displacement is based on the universal yield–bending–moment method (Xiong *et al.* 2017). As can be seen from Table 3, the ductility ratios range from 1.36 to 1.87.

4.1.5 Strength index

Strength index (*SI*) is able to quantify the utilization of capacity for composite walls and can be calculated by Eq. (2). As can be found in Table 3, the value of *SI* gradually increases with the growth in height-to-width ratio. The composite action between the steel faceplates and concrete core can be better realized with narrower walls. In an extreme case, the walls with smallest width can be considered as concrete-filled tube columns. Two reasons may contribute to the *SI* value larger than one. The first is due to the fact that the composite action enhances the load-carrying capacity, and the second is because that the possible contribution of steel truss is not considered in the calculation.

$$SI=\frac{N_u}{N_0} \tag{2}$$

$$N_y=f_yA_s+f_c'A_c \tag{3}$$

where N_0 is the fully-utilized capacity of the cross-section and can be calculated by Eq. (3). f_y and f_c' are the yield strength of steel and compressive strength of concrete core, respectively; A_s and A_c are the cross-sectional area of steel and concrete core, respectively.

4.2 Load versus lateral deflection curves

Figs. 12(a)-(c) shows the relationship between the axial load and the lateral deflection for each specimen. It can be seen that the lateral deflections on sides N and S at the same height are mostly symmetric. The curves gradually grow up as the axial loading increases until approaching the peak load. The lateral deflections then increase rapidly during the descending stage. It can also be observed that the in-plane deflection measured by transducer W19 during the axial

Table 2 Ductility ratio and strength index

Specimen No.	N_y	δ_y	$0.85N_u$	δ_m	μ	SI
	kN	mm	kN	mm		
SCW-2.0	7450	8.30	6800	12.11	1.46	0.96
SCW-2.5	6440	9.27	6182	17.30	1.87	1.08
SCW-3.3	5240	11.76	4945	16.03	1.36	1.13

compression tests is small and can be ignored.

The comparison among the load-lateral deflection curves at middle height of wall is shown in Fig. 12(d). It is obvious that the slope of load-lateral deflection curve is smaller for Specimen SCW-2.0 than for the other two specimens, which means the lateral deflections develop fastest in Specimen SCW-2.0. This is because the for double skin composite wall with boundary elements, weaker restraint is provided for wider walls to prevent the out-of-plane deformation.

4.3 Load versus strain curves

Similar trends can be found among strain development at different locations. In addition, the strain distributions exhibit no apparent differences among three specimens under the same level of loading before local buckling, which means the influence of height-to-width ratio on strain response is negligible. Therefore, only the load-strain relationship for Specimen SCW-2.0 is shown in Figs. 13. The strain goes up linearly with the growth in axial loading until the buckling of steel faceplate occurs. Furthermore, the increase rate in strain is relative smooth before reaching the peak loading. After that, the strain changes abruptly as the axial load starts to decrease in the descending period.

It is also interesting to see that, for the strains in the first row which is at a distance of 500 mm from the top of wall, the strain values at the center of wall are greater than those at the sides, while for the strains in the second row which is at a distance of 1000 mm from wall top, the strain values at the sides are greater than those at the center. For the strains in the third, fourth, and fifth rows, the strain values are mostly distributed uniformly. This indicates that the axial force concentrates at the center at the locations close to the loading point, and is transferred inclined to vertical direction to the sides. The axial force finally uniformly carried by the entire cross-section of the wall at the location far from the loading point.

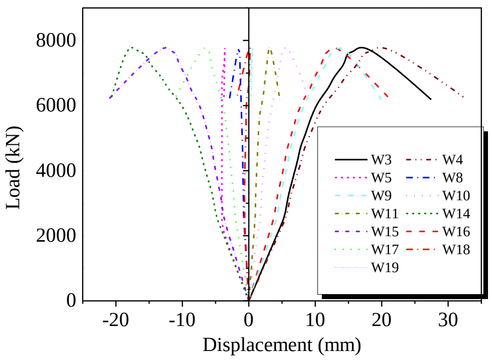

(a) Specimen SCW-2.0

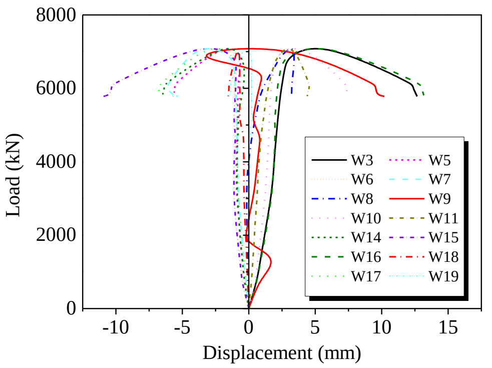

(b) Specimen SCW-2.5

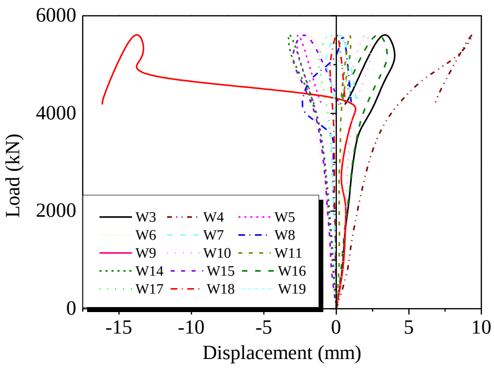

(c) Specimen SCW-3.3

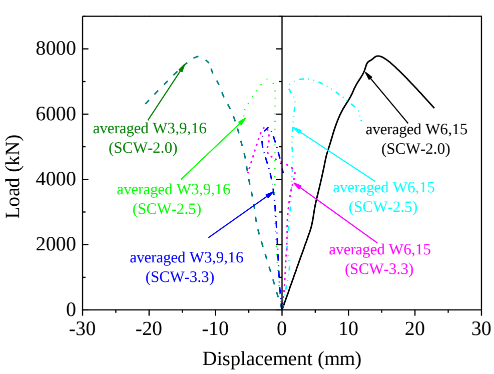

(d) Comparison of lateral deflection

Fig. 12 Load-lateral deflection curves

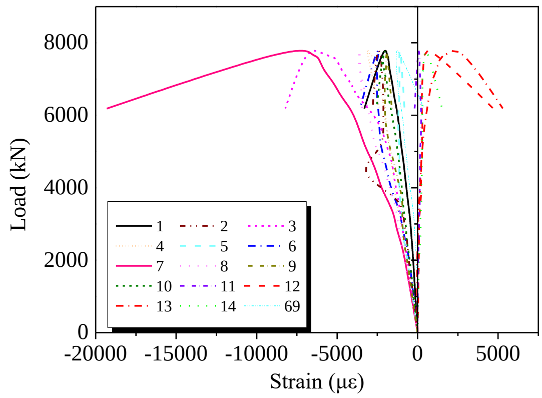

(a) The 1st row

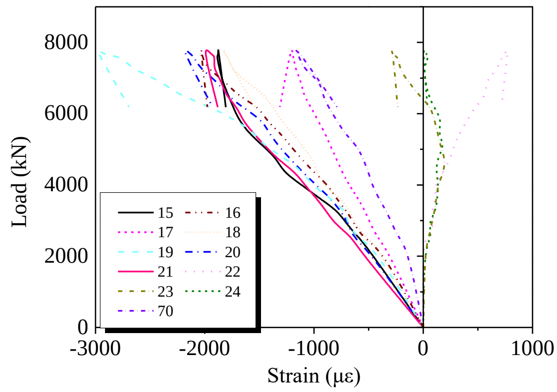

(b) The 2nd row

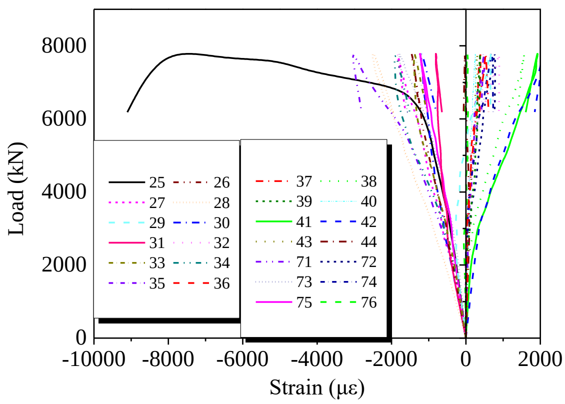

(c) The 3rd row

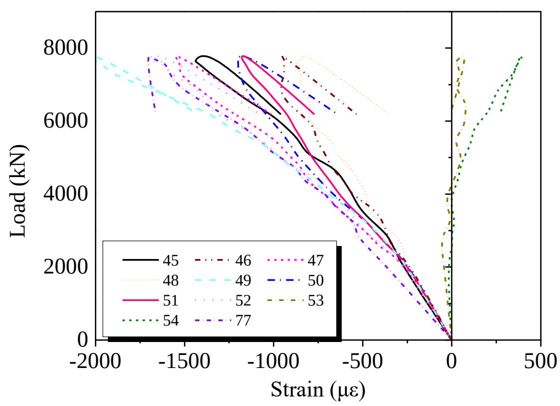

(d) The 4th row

Continued-

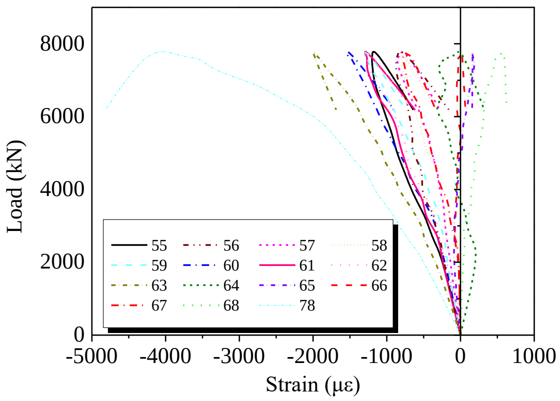

(e) The 5th row

Fig. 13 Load-strain curves for Specimen SCW-2.0

Table 3 Comparison with code-based prediction

Specimen No.	N_u	N_{AISC}	$\frac{N_u}{N_{AISC}}$	N_{EC4}	$\frac{N_u}{N_{EC4}}$
	kN	kN		kN	
SCW-2.0	8000	7165	1.12	7057	1.13
SCW-2.5	7273	5778	1.26	5717	1.27
SCW-3.3	5818	4382	1.33	4362	1.33
Average			1.23		1.25
Standard deviation			0.088		0.084

4.4 Code-based design

The predicted load-carrying capacities of the test specimens by AISC 360-16 (2016) and EN 1994-1-1:2004 (2004) are given in Table 4. It can be seen that the two modern codes generate similar predictions. The average ratio and standard deviation of test data to calculated results are 1.23 and 0.088, respectively, for AISC, while those are 1.25 and 0.084, respectively, for Eurocode 4. It can be concluded that both codes are on the safe side to determine the wall's loading capacity, though they both significantly underestimate the actual capacity. Furthermore, the test-to-predicted ratio increases obviously with the increase in height-to-width ratio. This may be attributed to the fact that composite action is better achieved for specimens with smaller width.

5. Conclusions

To enhance the composite action between the steel faceplates and the concrete core, a recently proposed innovative type of truss connector was used as the internal connector. The height-to-thickness ratio, which largely affect the restraint effect to the steel faceplates, was selected as the studied parameter. Three full-scale walls with the height of 3000 mm, the thickness of 150 mm, and varied widths were designed and tested under axial compression. The following conclusions are drawn based on the discussion in this research.

(1) The failure of three specimens includes the local buckling of steel faceplates and the subsequent global instability of the wall after reaching the peak load.

(2) For the walls with given height and thickness, the increase in height-to-width ratio results in the decrease in axial stiffness and the increase in strength index. Furthermore, greater height-to-width ratio leads to smaller lateral deflection under the same level of loading. The influences of height-to-width ratio on the buckling load, ductility and strain distribution is not significant.

(3) AISC 360 and Eurocode 4 offer similar predictions for the load-carrying capacity of composite walls. Both codes are over conservative to determine the actual strength.

Acknowledgments

This work is sponsored by the Natural Science Foundation of Jiangsu Province (Grant No. BK20170685), the National Key Research and Development Program of China (Grant No. 2017YFC0703802), and the Jiangsu Overseas Visiting Scholar Program for University Prominent Young & Middle-aged Teachers and Presidents, and the Fundamental Research Funds for the Central Universities (Grant No. 2242018K40137). The authors would like to thank the Zhejiang Southeast Space Frame Group Company Limited for the supply of test specimens, and Jian-Hong Han, Hui-Kai Zhang, Ke-Rong Luo, Shi Cao, and Rui Pan in the steel research group of Southeast University for their assistance with the laboratory work.

References

AISC 360-16 (2016), Specification for structural steel buildings, American Institute of Steel Construction, Chicago.

Akiyama, H. and Sekimoto H. (1991), A compression and shear loading tests of concrete filled steel bearing wall, *Transaction of 11th Structural Mechanics in Reactor Technology (SMiRT-11)*, 323-328.

GB 50010-2010 (2010), Code for design of concrete structures. China Architecture & Building Press, Beijing, 2010.

GB 50017-2017 (2017), Standard for classification of steel structures. China Architecture & Building Press, Beijing, 2017.

Choi, B.J. and Han, H.S. (2009), "An experiment on compressive profile of the unstiffened steel plate-concrete structures under compression loading", *Steel Compos. Struct.*, **9**(6), 519-534. https://doi.org/10.12989/scs.2009.9.6.519.

Choi, B.J., Kang, C.K. and Park, H.Y. (2014), "Strength and behavior of steel plate–concrete wall structures using ordinary and eco-oriented cement concrete under axial compression", *Thin Wall Struct.*, **84**, 313-324. http://dx.doi.org/10.1016/j.tws.2014.07.008.

Curkovic, I., Skejic, D., Dzeba, I. and De Matteis, G. (2019), "Seismic performance of composite plate shear walls with variable column flexural stiffness", *Steel Compos. Struct.*, **33**(1), 19-36. https://doi.org/10.12989/scs.2019.33.1.019.

EN 1994-1-1:2004 (2004), Eurocode 4: Design of composite steel and concrete structures-Part 1-1: General rules and rules for buildings. British Standards Institution, London, UK.

Eom, T.S., Park, H.G., Lee, C.H., Kim, J.H. and Chang, I.H. (2009), "Behavior of double skin composite wall subjected to in-plane cyclic loading", *J. Struct. Eng.*, **135**, 1239-1249. http://dx.doi.org/10.1061/(ASCE)ST.1943-541X.0000057.

Gheidi, A., Mirtaheri, M., Zandi, A.P. and Alanjari, P. (2011), "Effect of filler material on local and global behaviour of buckling-restrained braces", *Struct. Des. Tall Spec. Build.*, **20** (6), 700-710. https://doi.org/10.1002/tal.555.

Guo, Q. and Zhao, W. (2019), "Design of steel-concrete composite walls subjected to low-velocity impact", *J. Constr. Steel Res.*, **154**, 190-196. http://dx.doi.org/10.1016/j.jcsr.2018.12.001.

Hajimirsadeghi, M., Mirtaheri, M., Zandi, A.P. and Hariri-Ardebili, M.A. (2019), "Experimental cyclic test and failure modes of a full scale enhanced modular steel plate shear wall", *Eng. Fail. Anal.*, **95**, 283-288. http://dx.doi.org/10.1016/j.engfailanal.2018.09.025.

Hariri-Ardebili, M.A., Samani, H.R. and Mirtaheri, M. (2014a), "Free and Forced Vibration Analysis of an Infilled Steel Frame: Experimental, Numerical, and Analytical Methods", *Shock Vib.*, **2014**, 439591. http://dx.doi.org/10.1155/2014/439591.

Hariri-Ardebili, M.A., Rahmani-Samani, H. and Mirtaheri, M. (2014b), "Seismic stability assessment of a high-rise concrete tower utilizing endurance time analysis", *Int. J. Struct. Stab. Dyn.*, **14**(6), 1450016. http://dx.doi.org/10.1142/S0219455414500163.

Hilo, S.J., Badaruzzaman, W.H.W., Osman, S.A. and Al-Zand, A.W. (2016), "Structural behavior of composite wall systems strengthened with embedded cold-formed steel tube", *Thin Wall. Struct.*, **98**, 607-616. http://dx.doi.org/10.1016/j.tws.2015.10.028.

Huang, S.T., Huang, Y.S., He, A., Tang, X.L., Chen, Q.J., Liu, X.P. and Cai, J. (2018), "Experimental study on seismic behaviour of an innovative composite shear wall", *J. Constr. Steel Res.*, **148**, 165-179. https://doi.org/10.1016/j.jcsr.2018.05.003.

Huang, Z.Y. and Liew, J.Y.R. (2016), "Compressive resistance of steel-concrete-steel sandwich composite walls with J-hook connectors", *J. Contr. Steel Res.*, **124**, 142-162. http://dx.doi.org/10.1016/j.jcsr.2016.05.001.

JGJ/T 380-2015 (2015), Technical specification for steel plate shear walls. China Architecture & Building Press, Beijing.

Kanchi, M. (1996), Experimental study on a concrete filled steel structure Part 2 Compressive tests (1). *Summary of Technical Papers of Annual Meeting, Architectural Institute of Japan*, 1071-1072.

Lee, W., Kwak, H.G. and Hwang, J.Y. (2019a), "Bond-slip effect in steel-concrete composite flexural members: Part 1-Simplified numerical model", *Steel Compos. Struct.*, **32**(4), 537-548. https://doi.org/10.12989/scs.2019.32.4.537.

Lee, W., Kwak, H.G. and Kim, J.R. (2019b), "Bond-slip effect in steel-concrete composite flexural members: Part 2-Improvement of shear stud spacing in SCP", *Steel Compos. Struct.*, **32**(4), 549-557. https://doi.org/10.12989/scs.2019.32.4.549.

Liao, J.J. and Ma, G.W. (2018), "Energy absorption of the ring stiffened tubes and the application in blast wall design", *Struct. Eng. Mech.*, **66**, 713-727. http://dx.doi.org/10.12989/sem.2018.66.6.713.

Luo, Y.F., Guo, X.N., Li, J., Xiong, Z., Meng, L., Dong, N.C. and Zhang J. (2015), "Experimental research on seismic behaviour of the concrete-filled double-steel-plate composite wall", *Adv. Struct. Eng.*, **18**, 1845-1858. http://dx.doi.org/10.1260/1369-4332.18.11.1845.

Mirtaheri, M., Gheidi, A., Zandi, A.P., Alanjari, P. and Samani, H.R. (2011). "Experimental optimization studies on steel core lengths in buckling restrained braces", *J. Constr. Steel Res.*, **67**(8), 1244-1253. https://doi.org/10.1016/j.jcsr.2011.03.004.

Mirtaheri, M., Sehat, S. and Nazeryan, M. (2018). "Improving the behavior of buckling restrained braces through obtaining optimum steel core length", *Struct. Eng. Mech.*, **65**(4), 401-408. https://doi.org/10.12989/sem.2018.65.4.401.

Nguyen, N.H. and Whittaker, A.S. (2017), "Numerical modelling of steel-plate concrete composite shear walls", *Eng. Struct.*, **150**, 1-11. http://dx.doi.org/10.1016/j.engstruct.2017.06.030.

Prabha, P., Marimuthu, V., Saravanan, M., Palani, G.S., Lakshmanan, N. and Senthil, R. (2013), "Effect of confinement on steel-concrete composite light-weight load-bearing wall panels under compression", *J. Constr. Steel Res.*, **81**, 11-19. http://dx.doi.org/10.1016/j.jcsr.2012.10.008.

Qin, Y., Shu, G.P., Fan, S.G., Lu, J.Y., Cao, S. and Han, J.H. (2017), "Strength of double skin steel-concrete composite walls", *Int. J. Steel Struct.*, **17**, 535-541. http://dx.doi.org/10.1007/s13296-017-6013-9.

Qin, Y., Shu, G.P., Du, E.F. and Lu, R.H. (2018), "Buckling analysis of elastically-restrained steel plates under eccentric compression", *Steel Compos. Struct.*, **29**(3), 379-389. https://doi.org/10.12989/scs.2018.29.3.379.

Qin, Y., Shu, G.P., Zhou, X.L., Han, J.H. and He, Y.F. (2019a), "Height-thickness ratio on axial behavior of composite wall with truss connector", *Steel Compos. Struct.*, **30**(4), 315-325. https://doi.org/10.12989/scs.2019.30.4.315.

Qin, Y., Shu, G.P., Zhou, G.G. and Han, J.H. (2019b), "Compressive behavior of double skin composite wall with different plate thicknesses", *J. Constr. Steel Res.*, **157**, 297-313. https://doi.org/10.1016/j.jcsr.2019.02.023.

Qin, Y., Shu, G.P., Zhang, H.K. and Zhou, G.G. (2019c), "Experimental cyclic behavior of connection to double-skin composite wall with truss connector", *J. Constr. Steel Res.*, **162**, 105759. https://doi.org/10.1016/j.jcsr.2019.105759.

Qin, Y., Li, Y.W., Lan, X.Z., Su, Y.S., Wang, X.Y. and Wu, Y.D. (2019d), "Structural behavior of the stiffened double-skin profiled composite walls under compression", *Steel Compos. Struct.*, **31**(1), 1-12. https://doi.org/10.12989/scs.2019.31.1.001.

Qin, Y., Li, Y.W., Su, Y.S., Lan, X.Z., Wu, Y.D. and Wang, X.Y. (2019e), "Compressive behavior of profiled double skin composite wall", *Steel Compos. Struct.*, **30**(5), 405-416. https://doi.org/10.12989/scs.2019.30.5.405.

Qin, Y., Shu, G.P., Zhou, G.G., Han, J.H. and Zhou, X.L. (2019f), "Truss spacing on innovative composite walls under compression", *J. Constr. Steel Res.*, **160**, 1-15. https://doi.org/10.1016/j.jcsr.2019.05.027.

Qin, Y., Luo, K.R. and Yan, X. (2020a), "Buckling analysis of steel plates in composite structures with novel shape function", *Steel Compos. Struct.*, **35**(3), 405-413. https://doi.org/10.12989/scs.2020.35.3.405.

Qin, Y., Shu, G.P., Zhou, X.L., Han, J.H. and Zhang, H.K. (2020b), "Behavior of T-shaped sandwich composite walls with truss connectors under eccentric compression", *J. Constr. Steel Res.*, **169**, 106067. https://doi.org/10.1016/j.jcsr.2020.106067.

Qin, Y., Chen, X., Xi, W., Zhu, X.Y. and Chen, Y.Z. (2020c), "Compressive behavior of rectangular sandwich composite wall with different truss spacings", *Steel Compos. Struct.*, **34**(6), 783-794. https://doi.org/10.12989/scs.2020.34.6.783.

Qin, Y., Chen, X., Zhu, X., Xi, W. and Chen, Y. (2020d), "Structural behavior of sandwich composite wall with truss connectors under compression", *Steel Compos. Struct.*, **35**(2), 159-169. https://doi.org/10.12989/scs.2020.35.2.159.

Qin, Y., Chen, X., Zhu, X.Y., Xi, W. and Chen, Y.Z. (2020e), "Experimental compressive behavior of novel composite wall with different width-to-thickness ratios", *Steel Compos. Struct.*, **36**(2), 187-196. https://doi.org/10.12989/scs.2020.36.2.187.

Qin, Y., Chen, X., Xi, W., Zhu, X. and Chen, Y. (2020f), "Eccentric compressive behavior of novel composite walls with T-section", *Steel Compos. Struct.*, **35**(4), 495-508. https://doi.org/10.12989/scs.2020.35.4.495.

Seo, J., Varma, A.H., Sener, K. and Ayhan, D. (2016), "Steel-plate composite (SC) walls: in-plane shear behavior, database, and design", *J. Constr. Steel Res.*, **119**, 202-215. http://dx.doi.org/10.1016/j.jcsr.2015.12.013.

Usami, S., Akiyama, H., Narikawa, M., Hara, K., Takeuchi, M. and Sasaki N. (1995), Study on a concrete filled steel structure for nuclear plants (part 2). Compressive loading tests on wall members. *Transaction of 13th Structural Mechanics in Reactor Technology (SMiRT-13)*, August 13-18, Brazil, 21-26.

Xiong, Q.Q., Chen, Z.H., Zhang, W., Du, Y.S., Zhou, T. and Kang, J.F. (2017), "Compressive behaviour and design of L-shaped columns fabricated using concrete-filled steel tubes", *Eng. Struct.*, **152**, 758-770. https://doi.org/10.1016/j.engstruct.2017.09.046.

Yan, J.B., Wang, Z., Wang, T. and Wang, X.T. (2018), "Shear and tensile behaviors of headed stud connectors in double skin composite shear wall", *Steel Compos. Struct.*, **26**(6), 759-769. https://doi.org/10.12989/scs.2018.26.6.759.

Yan, J.B., Chen, A.Z. and Wang, T. (2019), "Developments of double skin composite walls using novel enhanced C-channel connectors", *Steel Compos. Struct.*, **33**(6), 877-889. https://doi.org/10.12989/scs.2019.33.6.877.

Zhao, W.Y., Guo, Q.Q., Huang, Z.Y., Tan, L., Chen, J. and Ye, Y.H. (2016), "Hysteretic model for steel–concrete composite shear walls subjected to in-plane cyclic loading", *Eng. Struct.*, **106**, 461-470. http://dx.doi.org/10.1016/j.engstruct.2015.10.031.

CC